

A simple and effective carrier lifetime characterization for semiconductor thin films

Bao Quy Le¹, Tuan Nguyen Van², Dat Tran Quang², Vi Le Dinh², Thin Pham Van², and Nguyen Cuc Thi Kim^{1,†}

¹Precision Engineering & Smart measurements Lab, School of Mechanical Engineering, Hanoi University of Science and Technology, 1 Dai Co Viet, 100000 Hanoi, Vietnam

²Department of Physics, Le Quy Don Technical University, 100000 Hanoi, Vietnam

Abstract: Minority carrier lifetimes τ are a fundamental parameter in semiconductor devices, representing the average time it takes for excess minority carriers to recombine. This characteristic is crucial for understanding and optimizing the performance of semiconductor materials, as it directly influences charge carrier dynamics and overall device efficiency. This work presents a development of PbS thin film deposited by thermal evaporation, at which the PbS thin film was further employed for structural, optical properties, and τ . Especially, the PbS film is probed with an in-house setup for identifying the τ . The procedure is to subject the PbS thin film with a flashlight from a light source with a middle rotating frequency. The derived τ in the in-house characterization setup agrees well with the value from the higher cost characterizing approach of photoluminescence. Therefore, the in-house setup provides additional tools for identifying the τ values for semiconductor devices.

Key words: semiconductors; minority carrier lifetime; open circuit voltage decay; PbS thin films

Citation: B Q Le, T N Van, D T Quang, V L Dinh, T P Van, and N C T Kim, A simple and effective carrier lifetime characterization for semiconductor thin films[J]. *J. Semicond.*, 2025, 46(7), 072101. <https://doi.org/10.1088/1674-4926/24090005>

1. Introduction

Minority carrier lifetimes (τ) are a critical parameter in semiconductor devices, representing the average duration for excess minority carriers to recombine^[1]. This parameter is intricately linked to the nature and scale of recombination processes within the semiconductor, playing a pivotal role in understanding device performance^[1]. The characterization of minority carrier lifetimes holds significant importance for several reasons: (i) Device efficiency: The efficiency of semiconductor devices, such as solar cells, is directly impacted by minority carrier lifetimes. Longer lifetimes lead to reduced recombination and enhanced efficiency. (ii) Recombination mechanisms: Understanding minority carrier lifetimes offers insights into dominant recombination mechanisms like Shockley–Read–Hall (SRH), Auger, and intrinsic or radiative recombination. This realization is crucial for optimizing device performance and minimizing defects; and last but not least. (iii) Material selection: Minority carrier lifetimes serve as an efficiency indicator for solar cells, influencing material selection for practical applications.

Numerous techniques have been developed for extracting lifetime parameters, detailed in references^[1–3]. It is however, ensuring reliable lifetime measurements remains challenging due to potential variations arising from diverse techniques and sample characteristics^[4]. Lifetimes obtained from configurations with epitaxial layers on substrates are notably influenced by geometric factors like layer thickness and interface properties. This geometry-dependent lifetime compo-

nent can significantly impact effective carrier lifetimes, even in highly pure materials.

The primary challenge lies in developing precise techniques for accurately measuring these effective lifetimes, interpreting the results correctly, and using cost-effective setup/measurement, as a focal point of this study. Unlike non-contact methods such as photoluminescence (PL) or microwave photoconductance decay (MPCD), the methodology in this research necessitates device fabrication with Ohmic contacts and establishing electrical connections for measurements. While non-contact methods are prevalent in the photovoltaic field, their application to other semiconductor devices is gaining traction. The conventional open circuit voltage decay (COVCD) method entails monitoring open-circuit voltage decay in a diode over time, a parameter directly linked to the minority carrier lifetime. This non-destructive, straightforward, cost-effective technique makes it an appealing choice for investigating and enhancing device performance.

On the other hand, time-resolved photoluminescence (TRPL) is a powerful technique that enables the tracking of photogenerated carrier decay in semiconductors over time, providing critical insights into minority carrier lifetimes and the underlying recombination mechanisms. In specific applications, adapting the COVCD methodology to enhance precision and flexibility becomes necessary. The approach presented in this study yields device-specific lifetime results in contrast to the spatially resolved data obtained from non-contact measurements. By comparing our modified open-circuit voltage decay (MOCVD) technique with PL measurements, this research addresses the challenge of selecting the most appropriate method for characterizing minority carrier lifetimes. Furthermore, the method described here is an adapta-

Correspondence to: N C T Kim, cuc.nguyenthikim@hust.edu.vn

Received 5 SEPTEMBER 2024; Revised 22 JANUARY 2025.

©2025 Chinese Institute of Electronics. All rights, including for text and data mining, AI training, and similar technologies, are reserved.

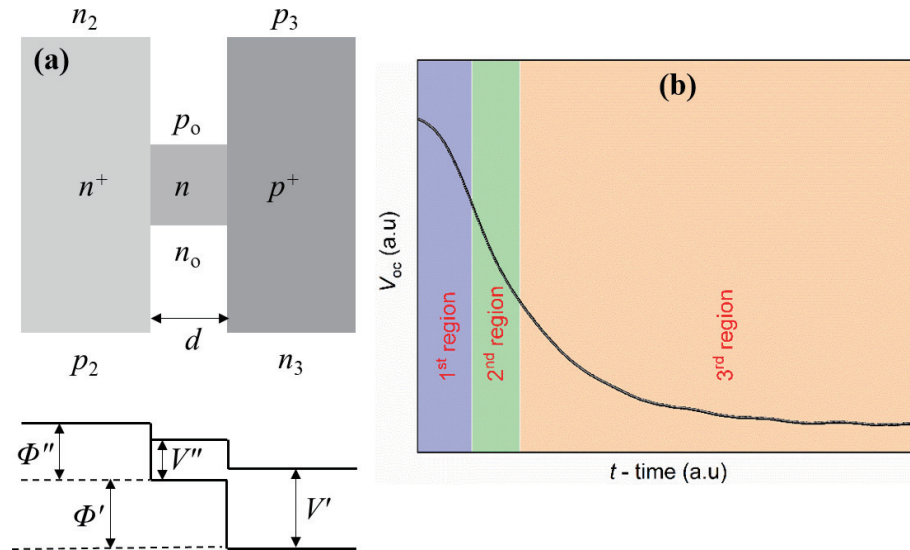


Fig. 1. (Color online) (a) The schematic of n^+ - p - p^+ diode in the forward biased steady state condition for establishing the theoretical background of the COCVD, and (b) the representatively theoretical OCVD curve at which three distinctive regions could be distinguished corresponding to different injection levels, i.e., high level (1st region), intermediate level (2nd region), and low level (3rd region).

tion of the open-circuit voltage (V_{oc}) decay technique originally introduced by Gossick^[5] and subsequently explored by several researchers^[6–10]. Gossick's technique involves generating excess minority carriers in a junction device through a brief forward current excitation, followed by monitoring the V_{oc} after the excitation is abruptly terminated. The minority carrier lifetime can be determined by analyzing the resulting V_{oc} decay curve. In this paper, we demonstrate that a flash of light, generated by a light source with a rotating chopper, can serve as an effective excitation source for V_{oc} decay measurements on suitably light-sensitive devices. The advantages of using light-induced excess carrier generation include that visible light more closely simulates the actual operating conditions of solar cells, and the experimental setup is remarkably straightforward. This approach not only enhances the accuracy of lifetime measurements but also simplifies the experimental process, making it a valuable tool for characterizing semiconductor devices.

2. Experimental details

2.1. Theoretical background

For establishing the theoretical background governing the COCVD in determining the minority carrier lifetime, start with an n^+ - p - p^+ diode operating under forward bias in a steady-state condition. This analysis is predicated on two primary assumptions:

(i) Junction modeling: The junctions formed by the diffusion of impurities into the silicon can be effectively represented as step junctions. This representation is valid when the impurity concentrations vary across four orders of magnitude within a distance of 10^{-4} cm from the junction interface. This significant variation in doping concentration allows for a simplified model that captures the essential physics of carrier movement across the junction.

(ii) Injection conditions: It is assumed that there is no injection of carriers into the highly doped regions at the levels considered in this analysis. This assumption simplifies the mathematical treatment of carrier densities across the junctions.

The populations of charge carriers on either side of these junctions can be described using Boltzmann distribution functions, which relate the electron and hole densities to their respective energy states and potential barriers^[8, 11]. The relation between these parameters presented in Fig. 1(a) can be expressed as:

$$\frac{n}{n_2} = e^{\omega(V''-\Phi'')} = \frac{n_0}{n_2} e^{\omega V''}, \quad (1)$$

$$\frac{p}{p_3} = e^{\omega(V'-\Phi')} = \frac{p_0}{p_3} e^{\omega V'}. \quad (2)$$

Here n (cm^{-3}), n_2 (cm^{-3}), n_0 (cm^{-3}), $\omega = q/k_B T$ (V^{-1}), V'' , V' , Φ'' , Φ' (cm^{-3}), p_3 (cm^{-3}), and p_0 (cm^{-3}) present the electron density in the conduction band, the conduction band at thermal equilibrium in the n^+ region, electron density in conduction band at thermal equilibrium in the base region, a parameter that relates charge, Boltzmann's constant, and absolute temperature, applied voltage across p - n^+ junction, applied voltage across p - p^+ junction, potential drop in thermal equilibrium across p - n^+ junction, thermal equilibrium potential drop across p - p^+ junction, hole density in valence band, hole density in valence band at p^+ region in thermal equilibrium, and hole density in valence band at thermal equilibrium in the base region, respectively.

At thermal equilibrium, when both applied voltages are zero ($V'' = V' = 0$) and when the electron and hole densities are equal to their thermal equilibrium values ($n = n_0$, $p = p_0$), both Φ'' and Φ' become negligible. Therefore, $np = n_0^2 e^{\omega V}$ with $V_{oc} = V' + V''$ (where n_i and V_{oc} are the number of carriers in intrinsic silicon and total voltage across diode, respectively). In the case considered, V_{oc} only accounts for voltage drops across the junctions themselves, excluding any contributions from carrier-carrier scattering within the base region^[12, 13]. Under these conditions, one can derive that: $p = n + N$. This equation is derived from the requirement of space charge neutrality in the base region.

This relationship arises from enforcing space charge neutrality within the base region, leading to a direct correlation

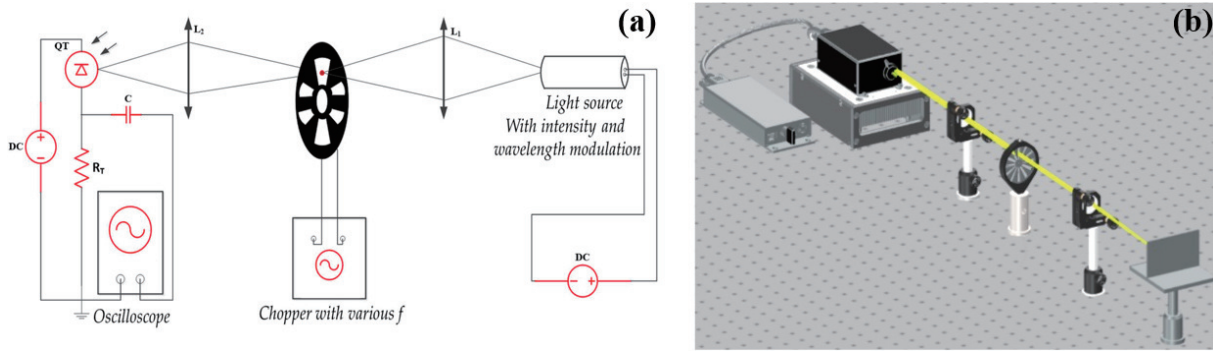


Fig. 2. (Color online) (a) The schematic developed MOCVD test setup, with detailed associated devices, and (b) the real 3D arranged component parts on the optical tray.

between voltage across a diode and electron density within that region. Thus, by monitoring voltage changes, one can infer variations in electron density. The lifetime of minority carriers in the base region is characterized by the following equation:

$$\frac{dn}{dt} = -\frac{n - n_o}{\tau}. \quad (3)$$

Here τ denotes the minority carrier lifetime. Given that one typically considers scenarios where $n \gg n_o$, and can neglect n_o , allowing us to rearrange our equations accordingly as follows:

$$dt = -\tau d\ln(n) \Rightarrow \tau = -\frac{dV}{d\ln(n)} \frac{dt}{dV_{oc}}. \quad (4)$$

Differentiating the above equation, one has:

$$\frac{d\ln(n)}{dV_{oc}} = \frac{\omega}{1 + \frac{n}{N}}. \quad (5)$$

Here d represents the width of the base region (cm), and N indicates uncompensated impurity concentration within that same region (cm^{-3}). Hence, in low injection conditions where $n \ll N$, $\tau = \frac{1}{\omega} \frac{dt}{dV_{oc}}$, at which the minority carrier concentration remains significantly lower than impurity levels. And conversely in high injection scenarios where $n \gg N$, $\tau = \frac{2}{\omega} \frac{dt}{dV_{oc}}$, for which minority carrier concentrations surpass impurity levels.

In the COCVD approach, the dependence of V_{oc} with respect to the time t is described in Fig. 1(b). In the decay mode, the plot for a device typically exhibits up to three discernible regions, as illustrated in Fig. 1(b). The initial zone signifies high-level injection denoted as the 1st region, for which the surplus minority carrier concentration surpasses the equilibrium majority carrier concentration in the cell's base region. During this phase, the decay curve appears linearly, allowing the derivation of the minority carrier lifetime τ through the above derived equation:

$$\tau = \left| \frac{2k_B T}{q} \frac{1}{\frac{dV_{oc}}{dt}} \right|. \quad (6)$$

Moving to the second segment of the decay curve, it

reflects an intermediate injection state corresponding to the 2nd region, of which the surplus minority carrier concentration in the base exceeds the thermal-equilibrium minority carrier concentration but falls short of the thermal-equilibrium majority carrier concentration. In this scenario, the decay curve maintains linearity, enabling the computation of the lifetime using the subsequent expression:

$$\tau = \left| \frac{k_B T}{q} \frac{1}{\frac{dV_{oc}}{dt}} \right|. \quad (7)$$

Concluding with the third segment of the decay curve, a state of low injection is illustrated by the 3rd region and characterized by the surplus minority carrier concentration being lower than the equilibrium minority carrier concentration. In this context, as V_{oc} becomes significantly smaller than $k_B T/q$, indicating a distinct low-injection regime^[5], and the V_{oc} approaches an exponential time dependence as follows:

$$V_{oc} = \frac{k_B T}{q} \left(e^{\frac{qV_o}{k_B T}} - 1 \right) e^{-\frac{t}{\tau}}. \quad (8)$$

Here V_o represents the open circuit voltage at the termination of excitation. This analysis relies on the premise of a one-sided junction, ensuring that the photovoltage contribution from the heavily doped emitter is insignificant. Additionally, it necessitates the excess charge stored in the space-charge region to be minimal compared to that in the base. Under these conditions, the decay is defined by the minority carrier lifetime in the base^[14].

2.2. The in-house MOCVD setup

The conventional semiconductor thin film has usually been deposited onto a substrate, i.e., from glass, silicon-based technology. And thus, the lattice mismatch between the employed substrate and the semiconductor films significantly influences the developed film properties. This means that the interfacial surface between the substrate and the film greatly contributes to semiconductor properties, i.e., organic solar cells. In order to characterize the developed film in a robust and accurate route, the MOCVD was developed, at which the V_{oc} can be increased and thus resulting in improving performance and efficiency.

In Fig. 2, the schematic illustration unveils the MOCVD in-house test setup devised to gauge the response time of a

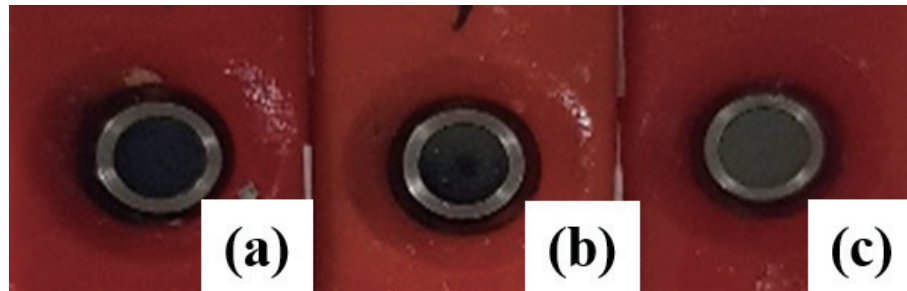


Fig. 3. (Color online) The three developed PbS photodetectors developed in this study (a), (b), and (c).

developed PbS photodetector. This apparatus comprises a luminous entity denoted as a light source, which derives its power from a customizable source. The radiance emanating from the light source travels through the converging lens L_1 , by which a modulation chopper strategically positioned at the focal point of L_1 engineers a square light pulsed beam. Subsequently, the light that permeates the modulation chopper is meticulously focused by lens L_2 before being cast upon the PbS photodetector. Upon exposure to these square light pulses, the photoresist induces a current in the circuit, which is so-called the photoelectric current. The resultant photocurrent signal is extracted from the load resistor R_T and observed on a digital oscilloscope.

The experimental MOCVD apparatus is illustrated in Fig. 2. The Stanford SR540 chopper modulator, boasting a frequency capability of up to 3.7 kHz with a resolution of 1 Hz, plays a pivotal role in this setup. Complementing this, the digital display oscilloscope Tektronix MDO 3012 Mixed Domain Oscilloscope is employed for precise observations and further recording data. It is noteworthy that the light source emits infrared radiation under the precise control of a Keithley 2231A DC source.

In the in-house setup, each single region in the MOCVD curve allows the extraction of the minority carrier lifetime by fitting with the corresponding of Eqs. (6)–(8), respectively. It is noted that, the Eq. (8), could be rewritten by separating into bi-exponential decay function, as follows:

$$V_{oc} = \frac{k_B T}{q} e^{\frac{qV_0}{k_B T}} e^{-\frac{t}{\tau_1}} - \frac{k_B T}{q} e^{-\frac{t}{\tau_2}} = A_1 e^{-\frac{t}{\tau_1}} + A_2 e^{-\frac{t}{\tau_2}}. \quad (9)$$

And finally, the minority carrier lifetime extracted in the third region could be expressed as:

$$\tau_{\text{average}} = \frac{A_1 \tau_1^2 + A_2 \tau_2^2}{A_1 \tau_1 + A_2 \tau_2}. \quad (10)$$

In order to validate the minority carrier lifetime of the developed sample, the measured data by in-house characterization will be then correlated with the extracted lifetime characterized by a standard photoluminescence (PL) approach. All the measurements in this work are conducted at room-temperature.

2.3. Characterizing structure

Lead sulfide (PbS) is widely recognized as a quintessential direct narrow bandgap semiconductor, characterized by a bandgap of approximately 0.41 eV at 300 K^[15]. This relatively low bandgap is a critical attribute that renders PbS particularly well-suited for a variety of applications in the fields of

infrared detection and photovoltaics such as infrared cameras and sensors used in various technological applications, including night vision and thermal imaging^[16]. Its ability to effectively absorb low-energy photons, specifically those within the infrared spectrum, proposing PbS as an ideal candidate for use in photodetectors and solar cells that are designed to operate in this wavelength range. Furthermore, it also exhibits a remarkably high absorption coefficient in the infrared region^[17]. This high absorption coefficient means that PbS can achieve substantial light absorption even when utilized in thin film configurations. Such an advantage is particularly beneficial for techniques like OCVD measurements, as it ensures that a significant number of charge carriers are generated upon illumination. It is therefore this study selecting the PbS material to investigate with the in-house MOCVD setup for characterizing the minority carrier lifetime.

The test structure used in this study has been deposited by using an evaporation approach on glass substrate, at room-temperature, at vacuum ambient pressure of 10^{-6} Torr, and with a nominal thickness of 100 nm. The starting binary powder PbS was purchased from Neyco company-France, of 5N in purity. The PbS thin film was further packaged into a photodetector and ready for MOCVD characterizations in Fig. 3.

3. Results and discussion

3.1. PbS thin film characterizations

The evaporated PbS thin films were characterized by X-Ray diffractometer in θ – 2θ configuration, of Cu–K_{α1} radiation. The diffraction pattern of the deposited film is displayed in Fig. 4(a). The observable diffraction peaks were indexed at 2θ of 25.11°, 45.27°, 50.13°, and 52.86° corresponding to (111), (022), (311), and (222) respectively, of which they belong to space group $Fm\bar{3}m$ with cubic structure—B₁ type (JCPDS reference card #05–0592). The sharp and well-defined peaks in the XRD profile are indicative of its crystalline nature, with a strong preferential orientation along the (111) direction, highlighting the anisotropic growth characteristics of PbS thin film. Furthermore, the absence of any secondary peaks associated with metallic clusters or impurities suggests an essential level of purity and quality in the films, free from defects or contaminants. This crystalline perfection and purity level is crucial for the thin film performance in various applications. In addition, the unit cell parameters for PbS system in this work are about 5.9633 Å for lattice constant, 212.06 Å³ for unit cell volume. These values agree with the parameters in previous studies^[18].

The broadening of Bragg reflection peaks is a well-estab-

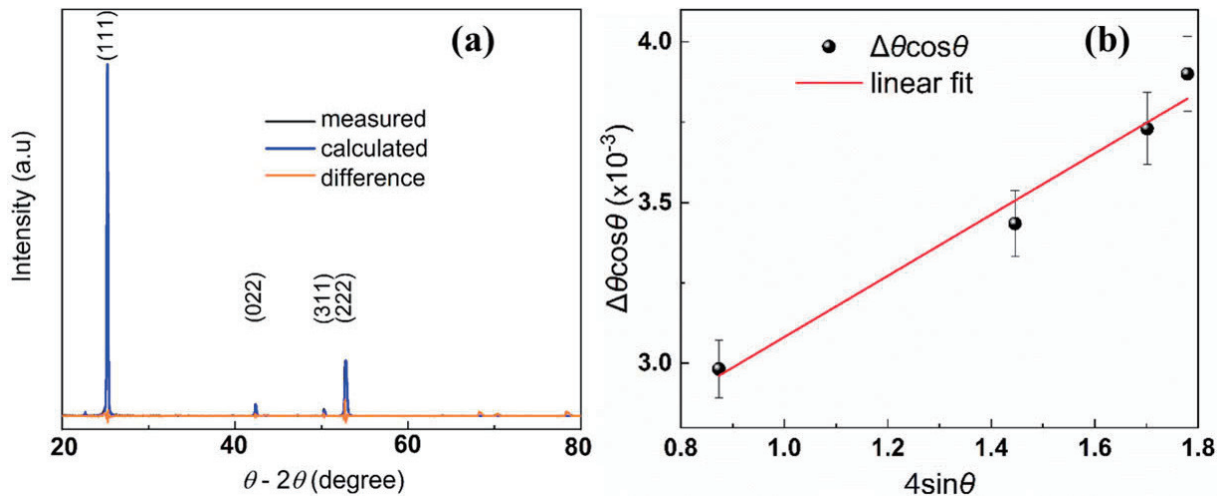


Fig. 4. (Color online) (a) The XRD pattern of the developed PbS thin film in the scanning range from 20° to 80°, and (b) the Williamson–Hall plot.

lished phenomenon that can induces changes to several derived parameters, including the reduction of crystallite size D and lattice strain η , which make the thin film properties different from its counterpart of the bulk one. To disentangle the individual contributions of D and η , this work employs the Williamson–Hall plot (WHP) method, a powerful analytical technique developed by Williamson and Hall^[19]. This approach allows for a quantitative assessment of the impact of crystallite size and lattice strain on the peak broadening, providing valuable insights into the microstructural properties of the material. By leveraging the WHP method, this study can gain a more nuanced understanding of the complex interplay between crystallite size, strain, and dislocation density, ultimately informing the design and optimization of materials for various applications.

The WHP could be expressed by the following relation:

$$\Delta\theta\cos\theta = \frac{K\lambda}{D} + 4\eta\sin\theta. \quad (11)$$

Here, $\Delta\theta$ is full width at half maximum of the diffracted peaks eliminating the broadening from instrumental contribution and this procedure has been described in previous study^[20], θ is angle of peak position, λ is the wavelength of the X-ray, D is average crystallite size, K is constant value 0.9 by presuming spherical nature and η is lattice strain. Plotting the $\Delta\theta\cos\theta$ as a function of $4\sin\theta$ allows to estimate the crystallite size from the intercept and lattice strain from the slope in Fig. 4(b). The calculated crystallite size and micro strain is about 65 nm and 0.095%. These derived values of D and η suggest that the deposited films are of nanocrystalline properties and obtain various degrees of strain.

Raman scattering is a powerful analytical tool that offers unique insights into the behavior of atomic clusters and the short-range order of nanostructure materials. In semiconductors, Raman scattering is primarily associated with longitudinal optical (LO) phonons, while other modes such as transverse optic (TO) and surface phonon (SP) are typically not observable due to symmetry restrictions and low intensities^[21, 22]. However, in nanostructure materials, the large surface-to-volume ratio enables the detection of SP modes through Raman scattering measurements, providing a valuable window into the surface properties of these materials. Moreover, Raman scattering is overly sensitive to even

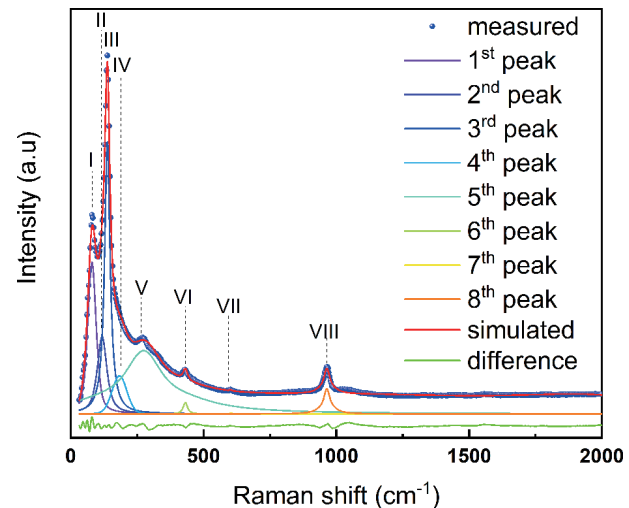


Fig. 5. (Color online) Raman spectroscopy of the PbS thin film, at which the Raman shift is deconvoluted into the componential peaks.

minute disorders, detecting small perturbations in the crystal lattice at scales as small as a few unit cells. This exquisite sensitivity makes Raman scattering an indispensable tool for probing the structural and electronic properties of a wide range of materials, from semiconductors to nanostructures.

Fig. 5 presents the Raman spectrum of deposited PbS thin film onto glass substrate when excited with a laser of wavelength 532 nm. While six peaks are directly observable, two additional hidden peaks are revealed through the deconvolution of the overall Raman spectra, denoted as peak II and peak IV. The transverse optical (TO) phonon mode for PbS thin films is indexed at 80 cm⁻¹^[21]. The interaction between different phonon modes gives rise to additional band signatures, i.e., peak II at 118 cm⁻¹ and peak III at 137 cm⁻¹, which might be tentatively attributed to longitudinal-transverse acoustic (LA-TA)^[23] and transverse acoustic (TA)-TO^[22] combination modes, respectively. A small shoulder, labeled as peak IV, corresponds to a surface phonon (SP) mode at 183 cm⁻¹^[22]. The dominant peak at 274 cm⁻¹ is assigned to the first-order fundamental longitudinal optical (LO) phonon mode^[23, 24], exhibiting an enhanced position due to the influence of nanocrystal size. The bands observed at 431 and 602 cm⁻¹ are associated with two-phonon (2LO) and three-phonon (3LO) scattering modes, respectively^[22, 25, 26].

Notably, the intensity of the first-order optical phonon process is significantly greater than that of the corresponding first and second overtones. The observed shifts to lower wavenumber values for 2LO and 3LO compared to their true values (548 cm^{-1} for 2LO and 822 cm^{-1} for 3LO), as noted in previous studies^[25], can be attributed to variations in grain size^[21] and/or the growth orientation of PbS films on glass substrates^[27]. Furthermore, the band at 961 cm^{-1} might indicate the presence of sulfates in the sample induced during the Raman investigation^[23]. In fact, the X-ray diffraction (XRD) pattern of the PbS confirms that the developed film consists solely of pure cubic PbS, with no detectable sulfates. Thus, the band at 961 cm^{-1} likely reflects sulfates resulting from laser-induced degradation, consistent with findings reported in earlier studies^[25]. The appearance of the SP mode is expected to exhibit characteristic behaviors: (i) an increase in surface-to-volume ratio correlating with a crystallite size of approximately 65 nm, and (ii) positioning between the TO and LO modes. Additionally, it is noteworthy that both TO and LO modes have shifted towards higher wavenumbers compared to previous studies, aligning well with the trend of increasing nanocrystalline size in thin films^[21]. The vibrational properties indicated in this study all relate to the belongings of PbS material, and thus it approves that the deposited PbS thin film is of decent quality.

At room temperature, optical absorption spectra of $1\text{ }\mu\text{m}$ PbS thin films have been studied to determine the absorption coefficient, optical band gap energy E_g and the nature of the transitions involved. The standard Beer's Law equation allows to estimate the variation of the transmitted intensity I with respect to the incident intensity I_0 as the following equation:

$$I = I_0 e^{-at}. \quad (12)$$

Here a is the absorption coefficient and t is the film thickness. And thus, the a value is estimated as:

$$a = -\frac{\ln\left(\frac{I}{I_0}\right)}{t} = -\frac{\ln(T)}{t}. \quad (13)$$

Here T represents transmittance PbS thin films.

Fig. 6 displays the dependence of transmittance and derived absorption coefficient spectra upon the wavelength of $1\text{ }\mu\text{m}$ PbS system. It is revealed that the transmittance edge is almost observed in the near infrared regime, i.e., the radiation beam is almost transmitted above 80% of the incident radiation in the range 2.5 to $8\text{ }\mu\text{m}$, and a significant drop of transmittance down to around 20% at around $10\text{ }\mu\text{m}$ and beyond. In addition, the derived absorption coefficient indicates that such transmittance reduction is attributed to the absorbance. This means that the radiation beam is absorbed, not reflected by the PbS semiconductor nature.

Since the PbS is of indirect band gap semiconductor, and thus the band gap values of the PbS samples obtained by the following formula^[28]:

$$(ahv)^{1/n} = \beta(hv - E_g). \quad (14)$$

Here hv , β , n , and E_g , represent the incident photon energy,

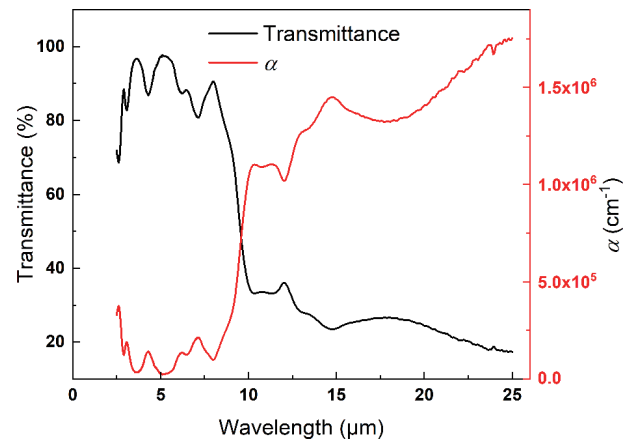


Fig. 6. (Color online) Transmittance and derived absorption coefficient spectra of $1\text{ }\mu\text{m}$ PbS thin film as function of the wavelength.

fixed constant, the power factor of the transition mode (dependent upon the nature of the material, i.e. crystalline or amorphous) and in this study $n = 2$ for indirect transition and band gap energy. Therefore, plotting $(ahv)^{1/2}$ versus the photon energy (hv) , gives a straight line in a certain region. The value of the indirect optical energy gap (E_g) may be calculated by extrapolating this straight line to intercept the (hv) -axis^[29].

The E_g values are estimated at about 0.45 eV, which is close to value of PbS bulk form (derived data not shown here). This value is much smaller of five folds compared to thinner thin films of less than 10 nm ^[30]. Literature suggests that increasing the thin film thickness up to a few tens nanometers results in the E_g value dropping to the bulk form one^[30]. Therefore, the obtained E_g value in this work agrees very well with the tendency from others' observations.

3.2. The compared PL measurement

Traditionally, assessing minority carrier lifetimes involves direct current (DC) photoconductive decay (PCD) measurements. Conversely, noninvasive and contact-free lifetime evaluations utilize time-resolved microwave reflectance (TMR) or time-resolved photoluminescence (TRPL) techniques. In TRPL, a brief laser pulse stimulates a light-emitting material, capturing the subsequent photoluminescence (PL) over time. The decay of emitted PL enables the extraction of carrier lifetimes. However, TRPL necessitates specialized optics and detectors tailored to the sample's emitted light wavelength. This often leads to the need for distinct optics and photodetectors for samples emitting across various electromagnetic spectrum regions. Moreover, TRPL involves trade-offs in detector selection, balancing sensitivity to enable the measurement of weakly emitting or small samples. In this work, the PbS thin films were stimulated by various laser radiation wavelengths, i.e., 363, 405, and 532 nm , from a NanoLog fluorescence spectrophotometer (Horiba, USA) excited by a 450 W Xenon lamp.

Analyzing TRPL data typically involves examining primary recombination mechanisms, including thermodynamic equilibrium, Shockley–Read–Hall (SRH) recombination, surface and interface recombination, Auger recombination, radiative recombination, and various aspects of light emission. To accurately analyze the radiative lifetime within TRPL data, it is essential to first define the total TRPL intensity from the vol-

ume V as an integral I_{TRPL} , expressed in the following relation^[31]:

$$\begin{aligned} I_{\text{TRPL}} &= B \int_V [(p_0 + \rho(r))(n_0 + \rho(r)) - n_i^2] dV \\ &= B \int_V [\rho(r)^2 + \rho(r)(p_0 + n_0)] dV. \end{aligned} \quad (15)$$

Here B , $\rho(r)$, p_0 , n_0 , and n_i represent a term that comes from summing the dipole matrix elements connecting the valence and conduction bands demonstrating specific to radiative recombination, the concentration of excess hole-electron pairs produced by the excitation, the free electron density, the free hole-density, and the intrinsic carrier density, respectively. Under steady-state excitation, $\rho(r)$ remains constant in time, and therefore I_{TRPL} remains constant. Under pulsed excitation, $\rho(r)$ decreases because of recombination and I_{TRPL} decays accordingly. This is the physical process basic to measuring the minority-carrier lifetime by TRPL. In a nondegenerate semiconductor, the equilibrium density of electron-hole pairs is constant at a given temperature. The law of mass action arising from thermodynamics and provide $np = n_i^2$ ^[32]. By assuming spatially uniform and instantaneous injection ρ_0 of electron-hole pair density, the radiative decay of ρ is given by:

$$\frac{d\rho}{dt} = -B(N\rho + \rho^2). \quad (16)$$

Here N is carrier density, and the I_{TRPL} per unit volume can be written as a function of time as $I_{\text{TRPL}}(t) = B[N\rho(t) + \rho(t)^2]$. At low-injection $\rho < N$, $I_{\text{TRPL}}(t)$ can be simplified to $I_{\text{TRPL}}(t) = BN\rho(t) = \frac{\rho(t)}{\tau_R}$ with radiative lifetime τ_R , and the $I_{\text{TRPL}}(t)$ linearly tracks the excess-carrier density $\rho(t)$. If nonradiative recombination mechanism with lifetime τ_{nR} is active in the material, the total lifetime τ and is given by the addition of the reciprocal lifetimes of $\frac{1}{\tau} = \frac{1}{\tau_R} + \frac{1}{\tau_{\text{nR}}}$, and the $I_{\text{TRPL}}(t)$ per unit volume is $I_{\text{TRPL}}(t) = \frac{\rho_0 e^{-\frac{t}{\tau}}}{\tau}$. At high injection in which ρ is not negligible compared to N , the $I_{\text{TRPL}}(t)$ must be evaluated by integrating Eq. (16) over the volume. It is obvious that the lifetimes in high injections are nonexponential for $t < \tau_R$. The minimum value of τ occurs at $t = 0$ and has the value $\frac{1}{\tau} = B(N + 2\rho_0)$. At very high injection ($\rho_0 \gg N$) and short times ($t \ll \tau_R$), The $I_{\text{TRPL}}(t)$ per unit volume versus time in this case is $I_{\text{TRPL}}(t) = \frac{B\rho_0^2}{(1 + B\rho_0 t)^2}$ ($t \ll \tau_R$) and the slope or instantaneous lifetime of the TRPL curve is $\tau = sd\frac{1}{2B\rho_0} + \frac{t}{2}$ ($t \ll \tau_R$). The TRPL data obtained at lower initial excess carrier densities can be temporally adjusted to align with equivalent carrier densities observed at higher initial levels. This method produces a combined photoluminescence curve that exhibits an improved signal-to-noise ratio during the later stages of signal decay.

Fig. 7 illustrates the combined TRPL signal for a 100 nm PbS thin film over time. Notably, a rapid initial decay is evident within the first 4 μs , followed by a slower decay for times greater than 4 μs . To elucidate the TRPL decay behavior, the minority carrier lifetime τ can be expressed in terms of its radiative and nonradiative components, specifically the

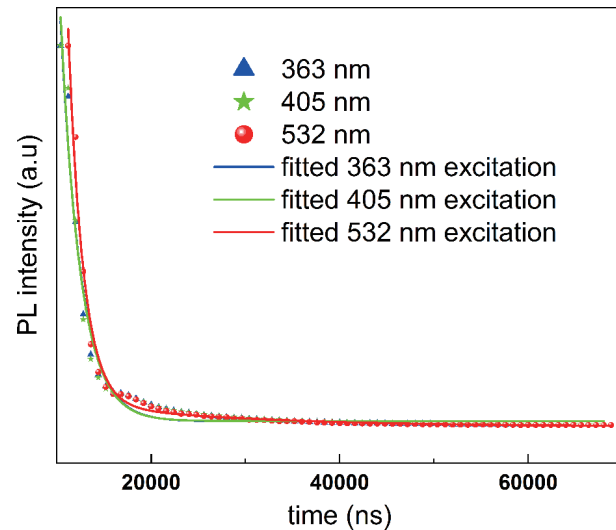


Fig. 7. (Color online) The TRPL signal over time for the 1 μm PbS thin film at various wavelength excitation.

Shockley–Read–Hall and Auger processes, as follows^[33]:

$$\frac{1}{\tau} = \frac{1}{\tau_{\text{SRH}}} + \frac{B}{\psi}\rho + C\rho^2. \quad (17)$$

Here τ_{SRH} is the Shockley–Read–Hall lifetime and ψ is the photon recycling coefficient. When ρ is small, the last two terms on the right side of Eq. (17) can be neglected, and, consequently, τ is assumed to be independent of ρ . As ρ becomes larger, contributions from radiative and Auger recombination can no longer be neglected, and the result is a decrease in the carrier lifetime. Therefore, a shorter lifetime followed by a longer lifetime is expected as ρ decreases, in agreement with the TRPL decay shown in Fig. 7. Effects on the fast initial decay due to surface recombination were neglected since no notable difference in the TRPL decay was observed when using excitation wavelengths of 363, 405, and 532 nm. Surface recombination effects would be stronger for shorter wavelengths.

The literature indicates that in PL measurement, the excitation wavelength does not significantly influence the decay dynamics^[34], as evidenced by the findings presented Fig. 7. This observation demonstrates the robustness of the PL technique across various excitation conditions. Typically, PL operates under low injection levels, where recombination events are primarily constrained by the concentration of minority carriers^[35–38]. In this scenario, both the total steady-state recombination rate and the resulting PL signal exhibit a direct proportionality to the carrier density. Moreover, when utilizing laser excitations with short wavelengths (< 500 nm), a narrow generation profile of charge carriers is created. This focused generation can lead to diffusion of the charge carriers away from the initial excitation area^[39, 40]. As a result, an initial drop in photoluminescence decay may occur, often manifesting as a bi-exponential decay pattern. This complexity can complicate data interpretation, making it challenging to extract accurate information about the underlying recombination processes^[41]. The calculated τ_{average} given by Eq. (10) is about 21.4, 20.9, and 15.8 μs with the excitation wavelength of 363, 405, and 532 nm, respectively. Obviously, the estimated τ_{average} is slightly dependent on the excitation wavelength of the source.

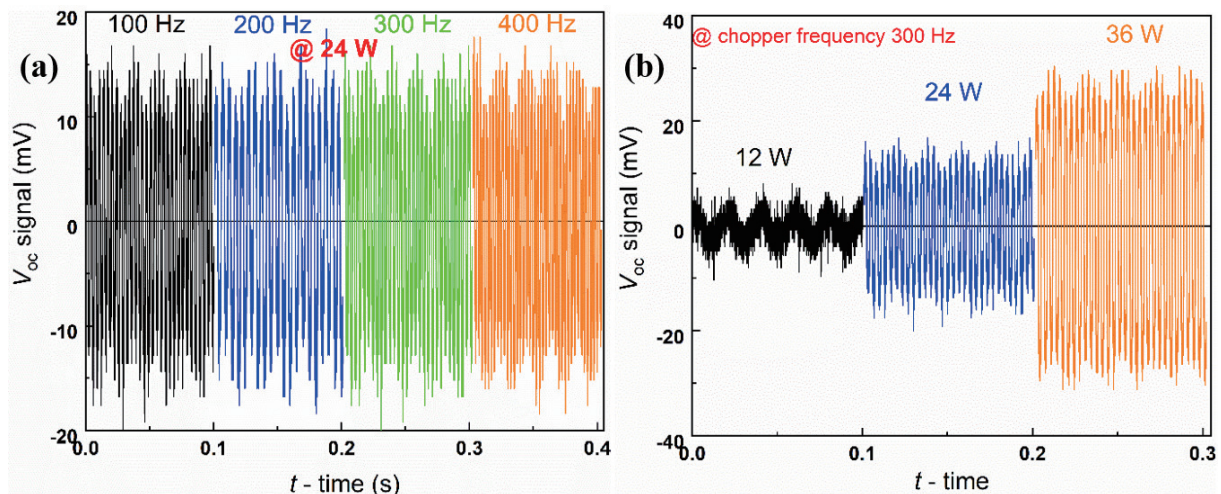


Fig. 8. (Color online) (a) The dependence of V_{oc} signal overtime at distinct chopper frequency ranging from 100 to 400 Hz, with power supply of 24 W to the light source, and (b) at various power supplies from 12 to 36 W at 300 Hz of chopper frequency.

3.3. The MOCVD characterization

In the in-house MOCVD setup, the frequency or power of the light source can be adjusted. Fig. 8(a) depicts the dependence of the open-circuit voltage V_{oc} signal on various chopper frequencies ranging from 100 to 400 Hz, with a constant light source power of 24 W, over a specific time period. Upon analyzing the V_{oc} signal over the scanning time, it is evident that the signal does not significantly depend on the introduced chopper frequency. This observation aligns well with the role of the chopper, which is to generate an alternating current (AC) signal for characterization purposes. The slight variations in the V_{oc} signal can be attributed to the real-time recording by the digital oscilloscope. They can be minimized by averaging a large number of data sets using the oscilloscope's built-in functions. In contrast, the V_{oc} signal is influenced by the light source power, as illustrated in Fig. 8(b). In this case, the chopper frequency was maintained at a constant value of 300 Hz while the light source power was varied by adjusting the supplied current and/or voltage. The V_{oc} signal exhibits a linear relationship with the light source power, with maximum values of approximately 8, 16, and 24 mV corresponding to light source powers of 12, 24, and 36 W, respectively. This behavior is expected, as the PbS thin film acts as a diode in this scenario.

In a diode, increasing the power of the incident beam leads to a higher number of photons approaching the diode, resulting in a higher V_{oc} signal. In practical applications, the V_{oc} signal may also be controlled by varying the wavelength of the light source and the temperature at which the experiment is conducted^[31, 33, 42]. In comparison between the PL and MOCVD approaches, the PL primarily involves the processes of surface emission and radiative recombination of charge carriers, whereas the MOCVD focuses on measuring carrier recombination and dynamic behavior within semiconductor materials. This distinction highlights that PL is often more sensitive to surface recombination phenomena, while the MOCVD tends to reflect the characteristics of bulk recombination. It is important to recognize that MOCVD is generally applied to bulk materials to investigate effective minority carrier lifetimes. For accurate extraction of minority carrier lifetimes from bulk materials, it is essential that the bulk

thickness is at least four times greater than the diffusion length^[4, 43]. In this study, 100 nm thick PbS thin film is deemed sufficient for characterization using the MOCVD approach. This thickness agree with findings from additional references which demonstrate that similar thin films characterized by COCVD can effectively achieve accurate minority carrier lifetime measurements^[44–46].

As previously discussed, the MOCVD technique can be categorized into three distinct zones, enabling the independent estimation of minority carrier lifetimes under high-level injection, intermediate injection, and low injection conditions. This in-house MOCVD setup is both simple and cost-effective compared to other methodologies, making it well-suited for these tasks. Figs. 9(a) and 9(c), present two representative curves from the MOCVD measurements, illustrating the three injection zones of high, intermediate, and low injection recorded using a digital oscilloscope. The fitting process for these curves, corresponding to the different injection stages, is depicted in Figs. 9(b) and 9(d), by which each injection stage is fitted with a distinct equation, as detailed in the previous section. For the data shown in Fig. 9(a), the minority carrier lifetimes τ at high, intermediate, and low injection levels are approximately 22.6, 19.4, and 18.5 μ s, respectively. In Fig. 9(c), the τ values are around 20.7, 18.9, and 17.7 μ s for high, intermediate, and low injection levels, respectively. It is important to note that Figs. 9(a) and 9(c), represent only two typical segments among thousands recorded during the measurement period.

To enhance the validation and reliability of the experimental results presented in this study, a careful analysis involving approximately 50 repetitions of distinct MOCVD curves to derive the minority carrier lifetimes corresponding to high, intermediate, and low injection levels is conducted, which are associated with the 1st, 2nd, and 3rd regions. Specifically, the mean minority carrier lifetime for each region was calcu-

lated using the formula $\bar{\tau} = \left(\sum_{i=1}^{50} \tau_i \right) / 50$, where τ_i represents the extracted minority carrier lifetime for the i th measurement period in the MOCVD curve. The error bars of $\Delta\tau = \left(\sum_{i=1}^{50} |\tau_i - \bar{\tau}| \right) / 50$ associated with these measurements

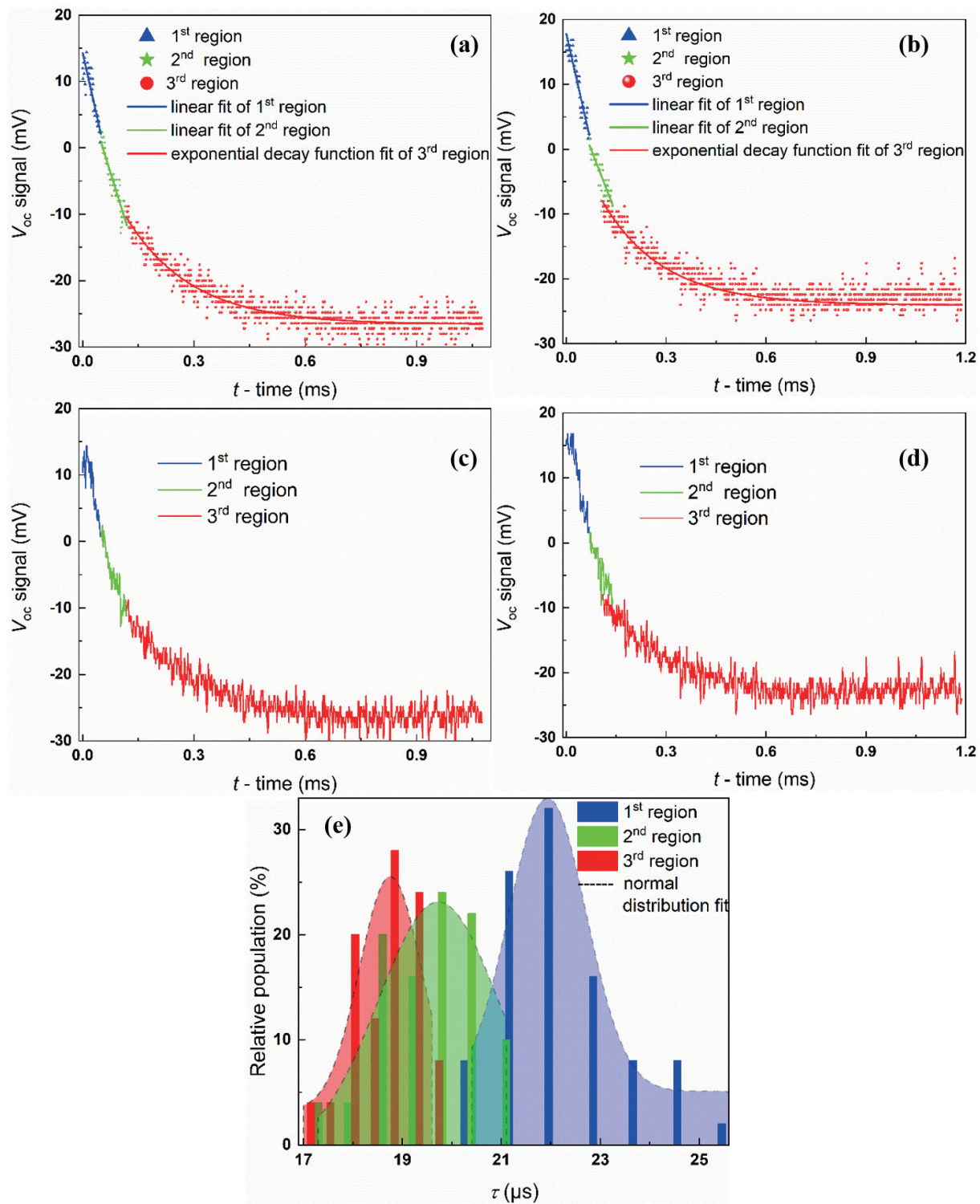


Fig. 9. (Color online) The analyzing process in the MOCVD setup. (a) and (c) The dependence of V_{oc} signal overtime at a scanning time; (b) and (d) typical regions in the OCVD curves corresponding to the fitting with either linear or bi-exponential decay function, which allows to indirectly estimate the minority carrier lifetimes of developed thin films; and (e) the statistical estimation for the minority carrier lifetimes derived from 50 MOCVD curves corresponding to the 1st, 2nd, and 3rd regions.

reflect the variability in the data. The calculated mean minority carrier lifetimes, along with their corresponding error ranges for 1st, 2nd, and 3rd regions, are approximately 21.8 ± 2.0 , 19.2 ± 1.6 , and $18.3 \pm 1.1 \mu\text{s}$, respectively. The statistical histogram of the derived minority carrier lifetimes across different regions conforms to a normal distribution (Fig. 9(e)). By disregarding systematic errors and applying a standard deviation σ , the accuracy with 2σ of the minority carrier lifetimes using the formula of accuracy = $\pm 2\sigma n^{-0.5}$, where $n = 50$ is the

number of derived minority carrier lifetimes. In this work, the σ values are determined of approximately 1.6, 2.4, and 1.3 for the 1st, 2nd, and 3rd regions, respectively. Consequently, the estimated accuracy of the derived τ values with 2σ is approximately $0.46 \mu\text{s}$ for the 1st region, $0.68 \mu\text{s}$ for the 2nd region, and $0.37 \mu\text{s}$ for the 3rd region. It is also noted that the τ values at each single region is significantly dependent on the route to select the linear or decay portion on the MOCVD curves and later derive for the τ . In short, the τ values derived

from our in-house MOCVD setup are coherent with those obtained from TRPL measurements corresponding to the 3rd region. This good agreement between the two approaches demonstrates that MOCVD approach is suitable for characterizing the τ of semiconductor materials.

The literature indicates that the carrier lifetime τ values in semiconductors can vary significantly, by several orders of magnitude, depending on factors such as purity and growth techniques. For example, in undoped silicon, the longest reported low-injection lifetime is approximately 20 ms^[47], while at high injection levels, a lifetime of 40 ms is achieved^[48]. Additionally, the τ value in silicon can exceed 100 μ s for Czochralski-grown wafers, which is orders of magnitude higher than that observed in thin film materials^[49]. Various methods have been employed to prepare PbS materials, each yielding different carrier lifetime characteristics. In nanoparticle form, PbS nanocrystals embedded within a polymer film exhibit a τ value of around 10 μ s as measured by time-resolved photoluminescence^[50]. This lifetime is comparable to that of PbS quantum dots encapsulated with tetrabutyl-ammonium iodide or ethanedithiol, as determined through impedance spectroscopy measurements^[51]. Notably, the τ value can be enhanced by an order of magnitude to 100 μ s for PbS quantum dot films, depending on the laser power applied during impedance spectroscopy characterization^[52]. In film form, with nanocrystalline properties achieved via chemical bath deposition on glass substrates, τ values can reach the millisecond scale as demonstrated by photoconductive decay techniques^[53], which is ten times higher than that observed in PbS layers deposited on sapphire substrates^[54]. Furthermore, depending on the characterization temperature, single crystal PbS films can yield a τ value of approximately 10 μ s when measured using a combination of photoconductivity and photomagnetic effects^[55]. By controlling dislocation density in PbS single crystals through chemical etching, a τ value of around 20 μ s has been reported based on photoelectromagnetic and photoconductive measurements^[56]. Evidently, the carrier lifetime obtained in this study aligns well with those reported for various other PbS materials.

The MOCVD offers a rapid and cost-effective method for characterizing semiconductor devices, particularly those that are commercially available off-the-shelf. One of the key advantages of MOCVD is its applicability to a diverse array of semiconductor materials, irrespective of their bandgap properties. This includes both wide and narrow bandgap semiconductors, as well as direct and indirect bandgap materials^[44]. Such versatility enables researchers and engineers to evaluate a wide variety of semiconductor types without being constrained by specific material characteristics, thus facilitating broader exploration and innovation in semiconductor technology. However, MOCVD has not been widely adopted for characterizing short carrier lifetimes due to certain inherent limitations. One significant drawback is that the technique necessitates the incorporation of electrical contacts along with a junction such as Schottky junction, which adds complexity to the experimental setup. This requirement can complicate the measurement process and may introduce additional variables that need to be controlled. Additionally, the signals obtained from MOCVD measurements can often be compromised by effects originating from the space charge region. These

effects include capacitive influences and generation/recombination currents that can obscure the true signal. As a result, the interpretation of the data may become blurred, leading to challenges in achieving accurate lifetime measurements^[57].

The MOCVD approach offers numerous advantages for characterizing semiconductor devices, particularly commercial off-the-shelf components. In this study, the digital oscilloscope integrated into the MOCVD setup is capable of capturing millions of data points across several thousand segments, as illustrated in Fig. 9. This capability significantly minimizes measurement errors, thereby enhancing the reliability of the results. Furthermore, our in-house MOCVD setup can be further optimized with integrated circuits specifically designed for big data processing. This enhancement allows for more accurate estimation of minority carrier lifetimes across various injection stages. The precision and robustness of this approach provide benefits comparable to those offered by photoluminescence techniques, while also being more cost-effective. As a result, this work paves the way for streamlined experimental procedures, establishing the MOCVD method as a vital tool for characterizing semiconductor devices. By integrating advanced data acquisition techniques and optimizing the setup for big data analysis, the approach is able to improve both the accuracy and efficiency of semiconductor characterization, ultimately contributing to advancements in the field.

4. Conclusions

Nominal 100 nm PbS thin films have been successfully fabricated using a thermal evaporation system at room temperature and an ambient pressure of 10^{-6} Torr. The structural and optical properties of the developed films were systematically characterized. Notably, the modified photo-induced open-circuit voltage decay technique has proven to be a robust and effective method for evaluating the base minority carrier lifetime in PbS thin films. Lifetimes obtained using the modified in-house setup show excellent agreement with results from alternative methods, such as photoluminescence characterization, thereby confirming the reliability of this approach. Furthermore, the modified in-house method offers a simplified characterization process and is more cost-effective compared to conventional techniques for determining minority carrier lifetimes. These findings indicate the importance of selecting appropriate measurement techniques and introduce a valuable tool for assessing the performance of PbS thin films and solar cells in general.

Acknowledgements

This research is funded by The Vietnam Ministry of Education and Training under project number B2024-BKA-12.

References

- [1] Schroder D K. Semiconductor material and device characterization. Wiley, 2005, 12
- [2] Diasso A, Sam R, Zouma B, et al. Experimental measurement of minority carriers effective lifetime in silicon solar cell using open circuit voltage decay under magnetic field in transient mode. Smart Grid Renew Energy, 2020, 11(11), 181

- [3] Li X X, He J H. A simplified formulation for calculation of minority-carrier effective lifetime. *Results Phys*, 2018, 11, 623
- [4] Lemaire A, Perona A, Caussanel M, et al. Open-circuit voltage decay simulations on silicon and gallium arsenide p-n homojunctions: Design influences on bulk lifetime extraction. *Microelectron J*, 2020, 101, 104735
- [5] Gossick B R. On the transient behavior of semiconductor rectifiers. *J Appl Phys*, 1955, 26(11), 1356
- [6] Choo S C, Mazur R G. Open circuit voltage decay behavior of junction devices. *Solid State Electron*, 1970, 13(5), 553
- [7] Wilson P G. Recombination in silicon p- π -n diodes. *Solid State Electron*, 1967, 10(2), 145
- [8] Davies L W. The use of P-L-N structures in investigations of transient recombination from high injection levels in semiconductors. *Proc IEEE*, 1963, 51(11), 1637
- [9] Ko W H. The reverse transient behavior of semiconductor junction diodes. *IRE Trans Electron Devices*, 1961, 8(2), 123
- [10] Bassett R J, Eulop W, Hogarth C A. Determination of the bulk carrier lifetime in the low-doped region of a silicon power diode, by the method of open circuit voltage decay. *Int J Electron*, 1973, 35(2), 177
- [11] Bassett R J. Observations on a method of determining the carrier lifetime in p+-v-n+ diodes. *Solid State Electron*, 1969, 12(5), 385
- [12] Davies L W. Electron-hole scattering at high injection-levels in germanium. *Nature*, 1962, 194, 762
- [13] Howard N R, Johnson G W. P + IN + silicon diodes at high forward current densities. *Solid State Electron*, 1965, 8(3), 275
- [14] Lindholm F A, Sah C T. Normal modes of semiconductor p-n-junction devices for material-parameter determination. *J Appl Phys*, 1976, 47(9), 4203
- [15] Liu S L, Fei G T, Xu S H, et al. High-performance visible-near IR photodetectors based on high-quality Sn 2+ -sensitized PbS films. *J Alloys Compd*, 2021, 883, 160860
- [16] Yin X T, Zhang C, Guo Y X, et al. PbS QD-based photodetectors: Future-oriented near-infrared detection technology. *J Mater Chem C*, 2021, 9(2), 417
- [17] Gao L F, Chen H L, Wang R, et al. Ultra-small 2D PbS nanoplatelets: Liquid-phase exfoliation and emerging applications for photo-electrochemical photodetectors. *Small*, 2021, 17(5), 2005913
- [18] Kumar S, Sharma T P, Zulfequar M, et al. Characterization of vacuum evaporated PbS thin films. *Phys B: Condens Matter*, 2003, 325, 8
- [19] Williamson G K, Hall W H. X-ray line broadening from filed aluminium and wolfram. *Acta Metall*, 1953, 1(1), 22
- [20] Van T N, Laborde E, Champeaux C, et al. Tunability of optical properties of InSb films developed by pulsed laser deposition. *Appl Surf Sci*, 2023, 619, 156756
- [21] Nanda K K, Sahu S N, Soni R K, et al. Raman spectroscopy of PbS nanocrystalline semiconductors. *Phys Rev B*, 1998, 58(23), 15405
- [22] Xiong S L, Xi B J, Xu D C, et al. L-cysteine-assisted tunable synthesis of PbS of various morphologies. *J Phys Chem C*, 2007, 111(45), 16761
- [23] Smith G D, Firth S, Clark R J H, et al. First- and second-order Raman spectra of galena (PbS). *J Appl Phys*, 2002, 92, 4375
- [24] Krauss T D, Wise F W. Raman-scattering study of exciton-phonon coupling in PbS nanocrystals. *Phys Rev B*, 1997, 55(15), 9860
- [25] Cao H Q, Wang G Z, Zhang S C, et al. Growth and photoluminescence properties of PbS nanocubes. *Nanotechnology*, 2006, 17(13), 3280
- [26] Krauss T D, Wise F W, Tanner D B. Observation of coupled vibrational modes of a semiconductor nanocrystal. *Phys Rev Lett*, 1996, 76(8), 1376
- [27] Rivera-Nieblas J O, Alvarado-Rivera J, Acosta-Enríquez M C, et al. Resistance and resistivities of pbs thin films using polyethylenimine by chemical bath deposition. *Chalcogenide Lett*, 2013, 10, 349
- [28] Tauc J. Amorphous and liquid semiconductors. *Boston, MA: Springer US*, 1974, 1
- [29] Shahane G S, More B M, Rotti C B, et al. Studies on chemically deposited CdS_{1-x}Se_x mixed thin films. *Mater Chem Phys*, 1997, 47(2/3), 263
- [30] Lee W, Dasgupta N P, Jung H J, et al. Scanning tunneling spectroscopy of lead sulfide quantum wells fabricated by atomic layer deposition. *Nanotechnology*, 2010, 21(48), 485402
- [31] Ahrenkiel, Richard K, Lundstrom M S. Chapter 2 minority-carrier lifetime in III-V semiconductors ed. *Academic Press Semiconductors and Semimetals*, 1993, 39, 39
- [32] Donahoe F J. Electronic semiconductors. *J Frankl Inst*, 1958, 266(5), 419
- [33] Connelly B C, Metcalfe G D, Shen H E, et al. Direct minority carrier lifetime measurements and recombination mechanisms in long-wave infrared type II superlattices using time-resolved photoluminescence. *Appl Phys Lett*, 2010, 97(25), 251117
- [34] Keitel R C, Brechbühler R, Cocina A, et al. Fluctuations in the photoluminescence excitation spectra of individual semiconductor nanocrystals. *J Phys Chem Lett*, 2024, 15(18), 4844
- [35] Bhosale J S, Moore J E, Wang X, et al. Steady-state photoluminescent excitation characterization of semiconductor carrier recombination. *Review of Scientific Instruments*, 2016, 87(1), 013104
- [36] Hariharan A, Schäfer S, Heise S J. Decay of excess carriers in a two-defect model semiconductor: A time-resolved photoluminescence study. *J Appl Phys*, 2021, 130(23), 235702
- [37] Krückemeier L, Krogmeier B, Liu Z F, et al. Understanding transient photoluminescence in halide perovskite layer stacks and solar cells. *Adv Energy Mater*, 2021, 11(19), 2003489
- [38] Endale G. Effects of transition energy on intra-band photoluminescence of zinc oxide (ZnO) semiconductor under low injection level. *Ujms*, 2019, 7(3), 35
- [39] Semyonov O, Subashiev A V, Chen Z C, et al. Photon assisted Lévy flights of minority carriers in n-InP. *J Lumin*, 2012, 132(8), 1935
- [40] Nguyen H T, Phang S P, Wong-Leung J, et al. Photoluminescence excitation spectroscopy of diffused layers on crystalline silicon wafers. *IEEE J Photovolt*, 2016, 6(3), 746
- [41] Kirchartz T, Márquez J A, Stolterfoht M, et al. Photoluminescence-based characterization of halide perovskites for photovoltaics. *Adv Energy Mater*, 2020, 10(26), 1904134
- [42] Dev S, Wang Y N, Kim K, et al. Measurement of carrier lifetime in micron-scaled materials using resonant microwave circuits. *Nat Commun*, 2019, 10(1), 1625
- [43] Lemaire A, Perona A, Caussanel M, et al. Open-circuit voltage decay: Moving to a flexible method of characterisation. *IET Circuits Devices Syst*, 2020, 14(7), 947
- [44] Sakata I, Hayashi Y. Open-circuit voltage decay (OCVD) measurement applied to hydrogenated amorphous silicon solar cells. *Jpn J Appl Phys*, 1990, 29(1A), L27
- [45] Gupta G K, Garg A, Dixit A. Electrical and impedance spectroscopy analysis of Sol-gel derived spin coated Cu₂ZnSnS₄ solar cell. *J Appl Phys*, 2018, 123(1), 013101
- [46] Price K, Cooper K, Lacy C. Open-circuit voltage decay in CdTe/CdS solar cells. *MRS Online Proc Libr*, 2005, 865(1), 533
- [47] Balarin M. Properties of silicon. EMIS datareviews series No. 4. einführung: C. hilsum, vorwort: T. H. Ning, INSPEC, the institution of electrical engineering, london, New York 1988, 31 kapitel, 1100 seiten, 260 datareviews, £ 195, ISBN 0-85296-4757. *Cryst Res Technol*, 1989, 24(4), 386
- [48] Yablonovitch E, Gmitter T. Auger recombination in silicon at low carrier densities. *Appl Phys Lett*, 1986, 49(10), 587

- [49] Bothe K, Sinton R, Schmidt J. Fundamental boron–oxygen-related carrier lifetime limit in mono- and multicrystalline silicon. *Progress Photovoltaics*, 2005, 13(4), 287
- [50] Lifshitz E, Sirota M, Porteanu H. Continuous and time-resolved photoluminescence study of lead sulfide nanocrystals, embedded in polymer film. *J Cryst Growth*, 1999, 196(1), 126
- [51] Speirs M J, Dirin D N, Abdu-Aguye M, et al. Temperature dependent behaviour of lead sulfide quantum dot solar cells and films. *Energy Environ Sci*, 2016, 9(9), 2916.
- [52] Rath A K, Lasanta T, Bernechea M, et al. Determination of carrier lifetime and mobility in colloidal quantum dot films via impedance spectroscopy. *Appl Phys Lett*, 2014, 104(6), 063504
- [53] Kotadiya N B, Kothari A J, Tiwari D, et al. Photoconducting nanocrystalline lead sulphide thin films obtained by chemical bath deposition. *Appl Phys A*, 2012, 108(4), 819
- [54] Espevik S, Wu C, Bube R H. Mechanism of photoconductivity in chemically deposited lead sulfide layers. 1971, 42(9), 3513
- [55] Batukova L M, Karpovich I A. Carrier lifetime in single-crystal PbS films. *Sov Phys J*, 1970, 13(6), 741
- [56] Scanlon W W. Lifetime of carriers in lead sulfide crystals. *Phys Rev*, 1957, 106(4), 718
- [57] Mahan J E, Barnes D L. Depletion layer effects in the open-circuit-voltage-decay lifetime measurement. *Solid State Electron*, 1981, 24(10), 989



Bao Quy Le received the B.E. (2008), M.E. (2010), degrees in mechanical engineering from Hanoi University of Science and Technology HUST, Vietnam. He is now a Ph.D student at HUST. He is interested in researching optical thin films and their applications in thermal imaging. He has experience working on interdisciplinary projects and wishes to contribute to the development of materials science and photonics.



Tuan Nguyen Van received the Ph.D. degree from Université de Limoges et Institut Néel-France, in 2021. He is currently a senior lecturer and researcher at Le Quy Don Technical University, Hanoi, Vietnam. His current research interests include research and applications of multiphase high-performance magnets, spintronics, magnetic sensors, and semiconductor devices.



Dat Tran Quang received his Ph.D. in 2018 from the Institute of Military Science and Technology, Vietnam. He is currently a Senior Lecturer and Head of the Laboratory at the Faculty of Technical Physics and Chemistry, Le Quy Don Technical University, Vietnam. His research focuses on advanced material synthesis and characterization using evaporation, sputtering, and CVD. He specializes in semiconductor optics and electronics, as well as materials for heavy metal ion adsorption and electromagnetic wave absorption.



Vi Le Dinh graduated with a Bachelor's degree in Engineering in 2011 from Belarusian State University of Informatics and Radioelectronics. He then earned his Master's degree in 2017 and his Ph.D. in 2020 from the same institution. Currently, Le Dinh Vi is a lecturer at Le Quy Don Technical University in Hanoi, Vietnam. His research focuses on semiconductor materials, nanoporous materials, and electronic devices.



Thin Pham Van obtained the Bachelor, Master, and Doctor degrees from VNU University of Science, in 1999, 2004, and 2015 respectively. He is now head of Department of Physics at Le Quy Don Technical University in Hanoi, Vietnam. He currently focuses on various topics including electronic devices, wide-range microwave absorbing materials, and infrared photodetectors.



Nguyen Cuc Thi Kim received the B.E. (2008), M.E. (2011), and Ph.D. (2019) degrees in mechanical engineering from Hanoi University of Science and Technology (HUST), Vietnam. She is currently a lecturer in the Department of Precision Mechanical and Optical Engineering, School of Mechanical Engineering of HUST. Her current interests include 3D accurate measurement, laser applications, semiconductor optics and devices, and medical instrument fabrication.